Research Article

Organic coating of 1–2-nm-size silicon nanoparticles: Effect on particle properties

Cristian R. Lillo[1], Juan J. Romero[1], Manuel Llansola Portolés[1,†], Reinaldo Pis Diez[2], Paula Caregnato[1], and Mónica C. Gonzalez[1] (✉)

[1] *Instituto de Investigaciones Fisicoquímicas Teóricas y Aplicadas (INIFTA), CCT-La Plata-CONICET, Facultad de Ciencias, Universidad Nacional de La Plata, cc 16, Suc. 4, 1900 La Plata, Argentina*
[2] *CEQUINOR, CCT-La Plata-CONICET, Facultad de Ciencias Exactas, Universidad Nacional de La Plata, cc 962,1900 La Plata, Argentina*
[†] *Present address: Department of Chemistry and Biochemistry, Center for Bioenergy and Photosynthesis, Arizona State University, Tempe, Arizona, USA*

ABSTRACT

Photoluminescent silicon nanoparticles 1–2 nm in size were synthesized by a wet chemical procedure and derivatized with propylamine (NH$_2$SiNP). Surface NH$_2$ groups were used as linkers for additional poly(ethylene glycol) (PEG) and folic acid (Fo) attachment (PEG–NHSiNP and Fo–NHSiNP, respectively) to enable efficient targeting of the particles to tumors and inflammatory sites. The particles were characterized by transmission electron microscopy, Fourier transform infrared spectroscopy, X-ray photoelectron spectroscopy, ζ potential, dynamic light scattering, and time-resolved anisotropy.

The photophysical properties and photosensitizing capacity of the particles and their interaction with proteins was dependent on the nature of the attached molecules. While PEG attachment did not alter the photophysical behavior of NH$_2$SiNP, the attachment of Fo diminished particle photoluminescence. Particles retained the capacity for ^{1}O$_2$ generation; however, efficient ^{1}O$_2$ quenching by the attached surface groups may be a drawback when using these particles as ^{1}O$_2$ photosensitizers. In addition, Fo attachment provided particles with the capacity to generate the superoxide anion radical (O$_2^-$).

The particles were able to bind tryptophan residues of bovine serum albumin (BSA) within quenching distances. NH$_2$SiNP and PEG–NHSiNP ground state complexes with BSA showed binding constants of $(3.1 \pm 0.3) \times 10^4$ and $(1.3 \pm 0.4) \times 10^3$ M^{-1}, respectively. The lower value observed for PEG–NHSiNP complexes indicates that surface PEGylation leads to a reduction in protein adsorption, which is required to prevent opsonization. An increase in particle luminescence upon BSA binding was attributed to the hydrophobic environment generated by the protein. NH$_2$SiNP–BSA complexes were also capable of resonance energy transfer.

🏛 **TSINGHUA** UNIVERSITY PRESS   ⌘ Springer

1 Introduction

Silicon nanoparticles (SiNP) 1–5 nm in size combine size-dependent photoluminescence, the capacity for $^1O_2$ generation, and diverse Si surface chemistry [1–3]. Surface modifications, such as coating/linking with folate, antibodies, adjuvants, and various other substances can increase particle solubility, biocompatibility, targeting potential, and circulation time in biological systems [4]. The latter properties are useful for bypassing biophysical barriers and preventing opsonization. Linking non-toxic poly(ethylene glycol) (PEG) reportedly prolongs the *in vivo* lifetime of drugs by preventing their macrophage-mediated uptake and removal from systemic circulation [5].

Preferential targeting of cancerous areas by NPs can be achieved via the increased permeation and retention effect (EPR) [6]. Besides being potentially useful for drug transport in chemotherapy, EPR can improve radiotherapy, since NPs can enhance the effects of radiation [7]; the role of SiNPs in potentiating the cytotoxic effects of radiation on cancer cells has been demonstrated [8, 9]. Delivering SiNPs specifically to tumor sites can minimize damage to healthy tissues while maximizing damage to cancer cells. The overexpression of folate receptor as a folate-binding protein is used to target drugs to cancer cells [10, 11]. Folic acid (Fo) bound to different substrates has receptor-binding capacity and endocytic properties. Thus, particle derivatization with Fo and PEG are predicted to provide efficient targeting to tumors and inflammatory sites.

However, there are challenges to using SiNPs as sensors and photosensitizers: Particle photoluminescence and cytotoxicity depend on size and crystallinity, but also on surface structure and chemistry [12, 13] as well as interaction with components of biological media [14, 15]. Nonetheless, through careful design it is possible to develop multifunctional NPs with potential applications in imaging, diagnosis, and therapy [16]. Herein we report the synthesis, characterization, and effect of surface groups on the photophysical properties, singlet oxygen-photosensitizing capacity, and protein interactions of a propylamine-derivatized SiNP and its derivatives functionalized with PEG and Fo.

Fetal bovine serum (FBS) was used to study the interaction of SiNPs with proteins in biological media,

since it is the most widely used growth supplement for cell culture [17]. Bovine serum albumin (BSA), the most abundant protein in FBS, has intrinsic fluorescence largely attributed to tryptophan residues, with minor contribution from numerous tyrosine residues. Tryptophan is highly sensitive to its local environment and can be used to measure changes in fluorescence emission spectra resulting from altered protein conformation by substrate binding and denaturation [18].

2 Experimental

2.1 Materials

Toluene (99.7%, H_2O 0.005%), methanol, cyclohexane, 9,10-diphenylanthracene (9,10-DPA), $LiAlH_4$ (95%), $SiCl_4$ (99%), ethyl ether (p.a. 99.9%), tetraoctylammonium bromide (TOAB, 98%), 2-propen 1-amine (AA), Fo, dicyclohexylcarbodiimide (DCC), N-hydroxysuccinimide (NHS), and PEG of average molecular weight ($<M_W> = 600 \pm 30$ (PEG_{14})) were purchased from Sigma-Aldrich (St. Louis, MO, USA) and used without further purification. KH_2PO_4, K_2HPO_4, and NaOH (99.99%) were from Merck (Whitehouse Station, NJ, USA). Tris-acetate-EDTA (TAE) buffer was prepared in the laboratory following established protocols [17].

Deionized water (> 18 MΩ·cm, < 20 ppb organic carbon) was obtained using a Millipore system (Billerica, MA, USA). Nitrogen (four-band quality) and oxygen gas were both from La Oxígena S.A. (Córdoba, Argentina).

The pH of SiNP suspensions in water was adjusted using different 0.1 M KH_2PO_4/K_2HPO_4 buffer solutions. Unless otherwise specified, particle suspensions were used at pH = 7.0. To study the effect of biological constituents on the photosensitizing properties of particles, inactivated FBS (Natocor, Córdoba, Argentina) was added to phosphate buffer particle suspensions.

2.2 Equipment and methods

Fourier transform infrared (FTIR) Spectra were obtained in the 4,000–400 cm^{-1} range with 1 cm^{-1} resolution on an Equinox spectrometer (Bruker, Billerica, MA, USA), using KBr disks or Si wafers as holders.

Attenuated total reflection (ATR)-IR spectroscopy Spectra were obtained on a Nicolet 380 FTIR ATR

accessory (Thermo Scientific, Waltham, MA, USA) with a ZnSe crystal and incident beam angle of 45°.

Absorbance measurements A double-beam UV-1800 spectrophotometer (Shimadzu, Kyoto, Japan) coupled to an integrating sphere was used for measurements, along with a quartz cuvette with an optical path length of 1 cm.

Photoluminescence Measurements were made on a Jobin Yvon Spex Fluorolog FL3-11 spectrofluorometer (Horiba Scientific, Edison, NJ, USA). For continuous irradiation experiments, the spectrofluorometer was equipped with an Xe lamp as the excitation source, a monochromator with a 1-nm bandpass gap for selecting excitation and emission wavelengths, and a red-sensitive R928 PM as a detector. Spectra were corrected for wavelength-dependent sensitivity of the detector and source; emission spectra were corrected for Raman scattering using the solvent emission spectrum. In all experiments, the temperature was maintained at ±0.1 °C using an F-3004 Peltier sample cooler with an LFI-3751 temperature controller (Wavelength Electronics, Bozeman, MT, USA). For time-resolved photoluminescence measurements, the fluorometer was equipped with a time-correlated single photon counting instrument with light-emitting diode excitation at 341 and 388 nm (full width at half-maximum, FWHM = ~400 ps). Data were globally fitted as the sum of exponentials and included instrument response deconvolution, until optimal values for χ^2, residuals, and standard deviation values were obtained.

Estimation of luminescence quantum yields (Φ_{em}) Emission spectra were collected at various excitation wavelengths. Identical measurements (excitation conditions, lamp energy, and spectrometer band-pass) were performed with 9,10-DPA in deaerated cyclohexane, which emits between 400 and 500 nm with a known efficiency of 90% upon excitation between 275 and 405 nm [1, 19]. The square of the ratio between refractive indices of solvents was used to correct for different media used in sample suspensions and the reference solution [18].

Time-resolved singlet oxygen phosphorescence detection Particle suspensions were irradiated with a Nd:YAG Surelite II laser (7 ns FWHM and 14 mJ per pulse at 355 nm) (Continuum, San Jose, CA, USA). The radiation emitted at 1,270 nm arising from the radiative relaxation of oxygen molecules from the lower excited singlet state to the ground triplet state was detected at right angles using an amplified Judson J 116/8sp germanium detector (5-mm diameter) (Teledyne Judson Technologies, Montgomeryville, PA, USA) after passing through appropriate filters. Typically, 64 laser shots were averaged to obtain signals with good signal-to-noise ratio. Because the experimental system was unable to detect traces below the 5-μs time range, $^1O_2$ emission in water (τ_Δ = 3.5 μs) could not be measured; therefore, either toluene or D_2O (τ_Δ = 68 μs) was used as a solvent. The signal intensity of the 1,270-nm traces generated by particle suspensions were compared to those of the reference 9,10-DPA [20] under a similar solution absorbance of 355 nm [18].

Steady-state $^1O_2$ generation and quenching Air-saturated aqueous suspensions of particles were irradiated in a closed vessel with a Rayonet lamp (Southern New England Ultraviolet Co., Branford, CT, USA) emitting at 350 ± 20 nm in the presence and absence of the $^1O_2$ scavengers furfuryl alcohol (FFA) and sodium azide. Oxygen concentration was measured throughout the reaction with an oxygen-sensitive electrode (Orion97-0899; Cole-Parmer, Vernon Hills, IL, USA).

Transmission electron microscopy (TEM) Micrographs were acquired with a 2010 F microscope (JEOL Ltd., Tokyo, Japan) using a carbon-coated 300-mesh copper grid. Images were analyzed using ImageJ software (National Institutes of Health, Bethesda, MD, USA). Particle diameters were determined assuming that the particle area obtained from TEM micrographs was the projection of a spherical particle. Due to poor contrast, 220 particles from different micrographs were manually selected for size analysis. Particle size distribution was described by a log-normal function.

X-ray photoelectron spectroscopy (XPS) Spectra were obtained under ultra-high vacuum with an XR50 spectrometer (Specs GmbH, Berlin, Germany) with Mg Kα as the excitation source and a PHOIBOS 100 half-sphere energy analyzer (Specs GmbH). Internal calibration was performed with Au 4f 7/2 (binding energy, BE = 84.00 eV) and with the adventitious C 1s

peak at BE = 284.4 eV. To obtain better insight into the chemical environment of different atoms, high-resolution XPS spectra were resolved by Gaussian–Lorentzian fitting until minimum χ^2 values were obtained.

Gel electrophoresis A 1% agarose gel in TAE buffer (pH = 8.0) was used as support along with 1% TAE buffer (pH = 8.0) as moving phase. Electrophoresis was carried out for 30 min at 100 V. SiNPs were detected by their photoluminescence upon irradiation with UV light provided by a SW06 filter.

Determination of H$_2$O$_2$ concentration H$_2$O$_2$ levels were measured with a commercial enzymatic colorimetric kit (Wiener Laboratorios S.A.I.C., Rosario, Argentina). Calibration curves were generated using commercial H$_2$O$_2$ standard solutions.

Bilinear regression analysis For low fluorophore absorbance (< 0.05), the steady state emission intensity at a given emission wavelength ($I(\lambda_{em})$) is proportional to the absorption coefficient of the fluorophore at the excitation wavelength ($\varepsilon(\lambda_{ex})$), the concentration of the fluorophore, and the factor $F(\lambda_{em})$ reflecting the shape of the emission spectrum. The bilinear regression analysis takes advantage of the linearity of $I(\lambda_{em})$ with respect to $\varepsilon(\lambda_{ex})$ and $F(\lambda_{em})$ to retrieve information from the experimental excitation–emission matrix on the minimum number of species and their relative emission and excitation spectra [21].

2.3 Synthesis routes

SiNP synthesis involved an adaptation of the LiAlH$_4$ reduction of SiCl$_4$ in the presence of TOAB reverse micelles [21, 22]. Freshly prepared particles showing H- and Cl-passivated surfaces were immediately surface-derivatized to avoid Si oxidation to Si–OH.

Propylamine functionalization Several approaches exist for the derivatization of freshly prepared particles with AA [22–24]; photo-initiated silylation was used here, involving the mixing of a colloid dispersion in toluene with μL quantities of AA (reactant in defect). The resultant suspension was irradiated for 5 h with a 254-nm light from eight Rayonet Lamps (RPR2537A; Southern New England Ultraviolet Co.) to yield NH$_2$SiNP. The particles were transferred to water by

solvent evaporation and redispersed in an ultrasound bath to obtain stable aqueous dispersions. Long sonication time was avoided to prevent surface oxidation.

Fo functionalization Fo (10 mg), NHS (2.5 mg), and DCC (3.3 mg) were dissolved in dimethylsulfoxide (4 mL) and added slowly to an NH$_2$SiNP aqueous suspension (5 mL, 1.5 mg·mL^{-1}). The reaction mixture was left in the dark with vigorous stirring for 12 h. The conjugated Fo–NHSiNP was purified by dialysis against deionized water and stored at room temperature in the dark.

Polyethylene glycol functionalization The procedure involved adding carboxyl (COOH)-terminated PEG to NH$_2$SiNP to obtain PEG–NHSiNP particles that were PEG-functionalized through an amide link. PEG–COOH was first synthesized by bringing to reflux a solution of PEG$_{14}$ (6.6 g) and succinic anhydride (4.4 g) in dry tetrahydrofuran (THF; 50 mL). After 12 h of reflux, the mixture was treated with cold ether to precipitate unreacted PEG and its mono- and dicarboxylated derivatives. The precipitate was further dissolved in THF containing NHS and DCC (4.6 and 5.2 mg, respectively, per 0.04 mmol HCO$_2$–PEG) and stirred for 12 h. The resultant solution was added to the NH$_2$SiNP water suspension and stirred vigorously for 12 h. Excess reactants were removed by dialysis against deionized water.

2.4 Nanoparticle modeling methods

Nanoparticles containing 17, 29, 35, 47, 71, 87, 99, 123, 141, 153, 161, 185, 209, 221, 227, 236, and 240 Si atoms in their core were modeled as portions of crystalline bulk Si, in which the Si–Si bond length was initially set to 2.35 Å. These particle sizes roughly corresponded to particle diameters between 0.7 and 2.2 nm.

SiNP geometry was optimized and the coordination number of every Si atom was calculated for optimized NPs. To calculate coordination numbers, a relaxation of up to 10% was considered for equilibrium Si–Si bond distances; that is, two Si atoms were considered bonded when they were separated by < 2.60 Å. Si atoms with coordination numbers < 4 were considered as surface atoms and were candidates for functionalization.

Calculations were carried out using the self-consistent–charge density–functional tight-binding

method [19] with the aid of the dftb+ program [25, 26]. Geometries were considered convergent when the maximum element of the gradient vector of the energy with respect to nuclear coordinates was < 0.01 au. The tolerance for charge self-consistency was fixed at 0.001 au.

3 Results and discussion

SiNPs 1–2 nm in size were obtained by adapting a bottom–up approach [21, 23, 27, 28], which yielded H-passivated NPs with Si–H and Si–Cl surface groups. These were derivatized with AA to obtain SiNPs with surface propylamine groups (NH$_2$SiNP) that were used as linkers for PEG and Fo attachment. Scheme 1 summarizes the synthesis pathways and surface chemistry of NH$_2$SiNP, Fo–NHSiNP, and PEG–NHSiNP.

3.1 Particle characterization

An average particle size of 1.6 ± 0.6 nm was estimated from TEM micrographs of NH$_2$SiNP (Fig. 1), which was within the experimental error and consistent with the size obtained from anisotropy experiments.

The FTIR spectrum of NH$_2$SiNP (Fig. 2(a), top) showed N–H vibrations at 3,400 cm^{-1} and 1,650–1,580 cm^{-1}, which are characteristic of primary amines. The bands at 1,450 and 1,250 cm^{-1} corresponding to Si–C deformation in Si–CH$_2$ and the peaks in the 2,930–2,890 cm^{-1} region due to CH$_2$ stretching and bending confirmed the presence of propylamine groups on the surface of NH$_2$SiNPs [29]. Peaks at 1,020–1,100 cm^{-1} corresponded to C–N stretching of primary amines [30]. However, since peaks at around 1,040–1,115 cm^{-1} are also characteristic of Si–O–Si vibrations [12], surface oxidation as a result of aging could not be excluded. The XPS spectrum of NH$_2$SiNP (Fig. 1(b)) showed Si 2p signals at 99.6 eV (27%), 100.8 eV (37%), and 101.6 eV (37%), characteristic of Si^0, Si–C, and Si$^+$ environments, respectively [31]. The C 1s signal at 282.7 eV implied the formation of Si–C bonds [31]. N 1s signals at 399.4 and 401.4 eV were assigned to C–NH$_2$ and C–NH$_2^+$X$^-$ bonds, respectively [31]. Si 2p signals at 103.0 eV and O 2s signals at 533.0 eV—which are characteristic of SiO$_2$ groups—were
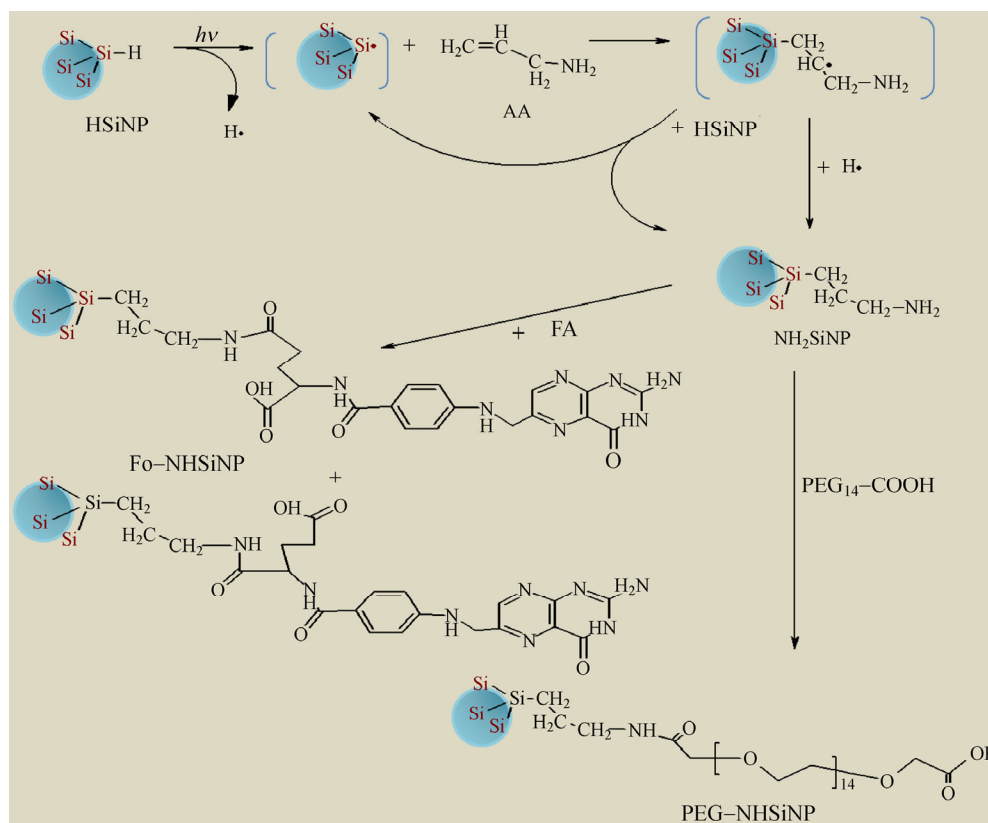
Scheme 1   Synthesis pathways and surface chemistry of NH$_2$SiNP, Fo–NHSiNP, and PEG–NHSiNP.
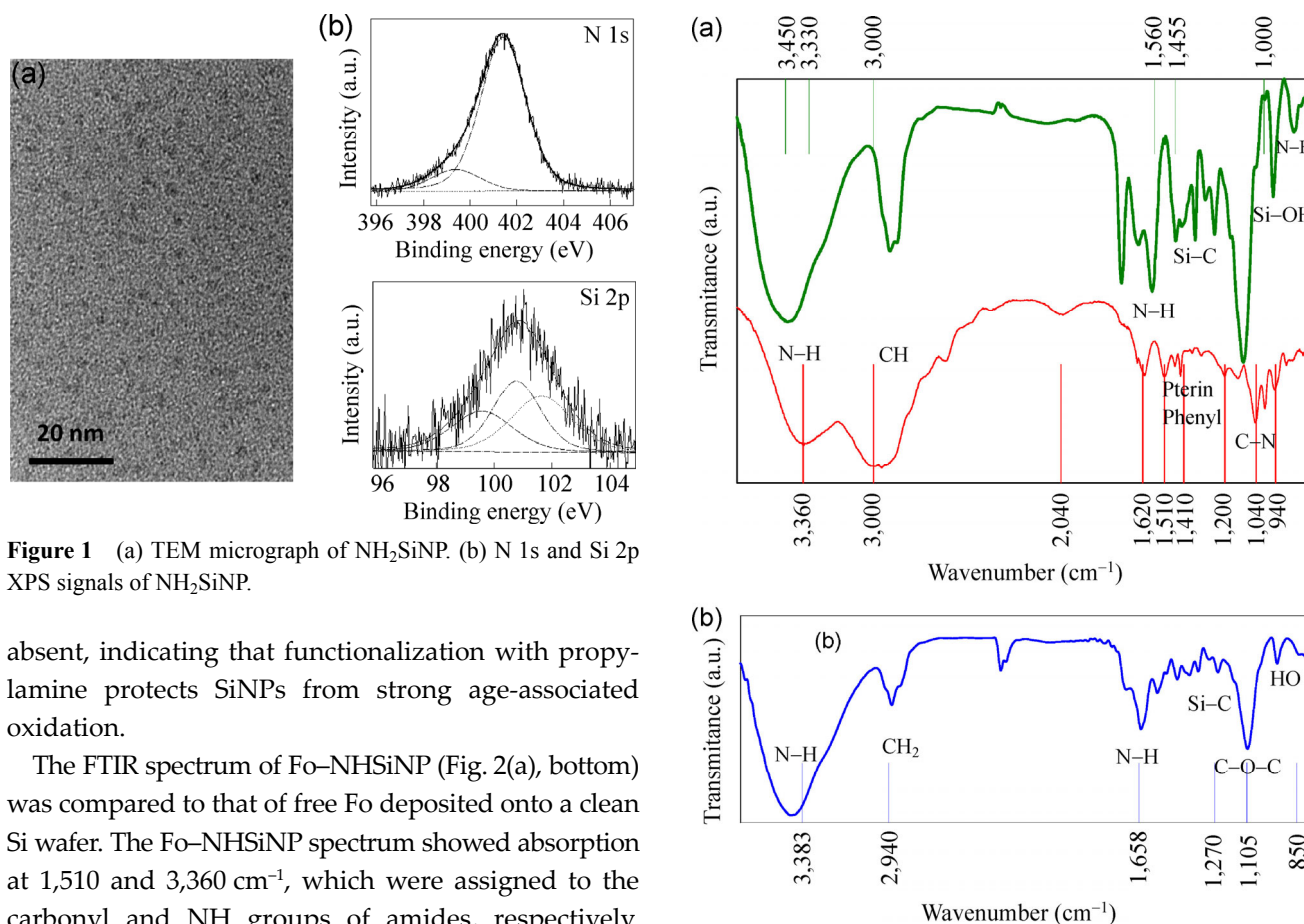
Figure 1 (a) TEM micrograph of NH₂SiNP. (b) N 1s and Si 2p XPS signals of NH₂SiNP.

Figure 2 FTIR spectra obtained using KBr disks as holders. (a) NH$_2$SiNP (top) and Fo–NHSiNP (bottom). (b) PEG–NHSiNP.

absent, indicating that functionalization with propylamine protects SiNPs from strong age-associated oxidation.

The FTIR spectrum of Fo–NHSiNP (Fig. 2(a), bottom) was compared to that of free Fo deposited onto a clean Si wafer. The Fo–NHSiNP spectrum showed absorption at 1,510 and 3,360 cm^{-1}, which were assigned to the carbonyl and NH groups of amides, respectively. Characteristic Fo bonds at 1,450 and 1,410 cm^{-1} due to C=C bonds in phenyl and pterin rings, respectively, were also observed [32]. The absorption bands at 3,000 and 2,940 cm^{-1} were assigned to C–H stretching in aromatic and alkyl groups, respectively. The peaks at 1,030 and 997 cm^{-1} were due to C–O deformation in –CONH–.

The FTIR spectrum of PEG–NHSiNP (Fig. 2(b)) showed characteristic bands at 2,960–2,850, 1,150–1,050, and 950 cm^{-1} due to C–H, C–O–C, and C–OH, respectively, in polyethylene glycol derivatives [33]. Moreover, intense peaks at 1,740–1,660 cm^{-1} corresponding to C=O stretching vibrations in acids and amides, as well as a peak at 3,480 cm^{-1} due to NH in amides, were also observed. The small peak at 1,250–1,270 cm^{-1} was attributed to Si–C vibrations.

Different running directions for NH₂SiNP and Fo–NHSiNP were observed by gel electrophoresis (Fig. 3(a)), as expected for the change in surface charge arising from NH$_3^+$ groups in NH₂SiNP and COO$^-$ in Fo–NHSiNP, confirming the efficient functionalization of

NH₂SiNP with Fo. On the other hand, PEG–NHSiNP remained in the seeding channel, indicating neutral coverage, in agreement with a measured ζ potential of 0.7 ± 4 mV. Average hydrodynamic particle size distribution as determined by dynamic light scattering (DLS) was several fold higher than that observed in TEM micrographs or determined by anisotropy experiments (Table 1), indicating particle aggregation in the aqueous solution. The nature of surface groups strongly influences aggregation; smaller aggregates were observed for Fo–NHSiNP and NH₂SiNP, consistent with their higher surface charge.

3.2 Particle modeling

SiNP modeling was performed to determine the number of surface Si atoms that were amenable to functionalization. This information allows the average molar mass of the particles and thus, of the particle
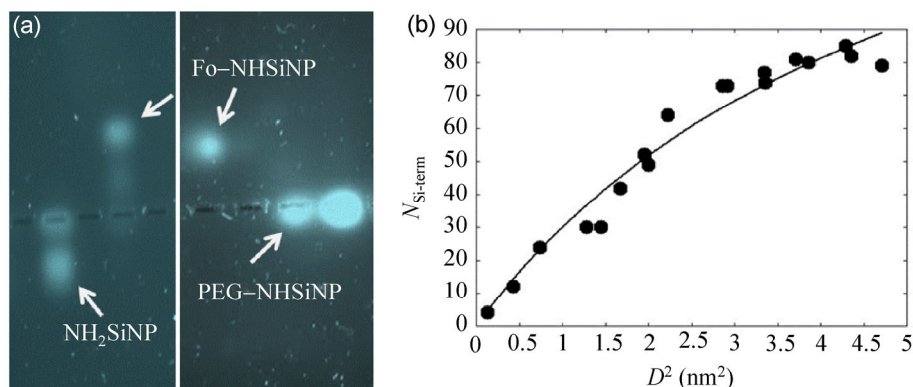
Figure 3 (a) Agarose gel electrophoresis of NH$_2$SiNP (lane 1 from left), Fo–NHSiNP (lanes 2 and 3), and PEG–NHSiNP (lanes 4 and 5). (b) Plot of computer-modeled $N_{\text{Si-term}}$ vs. D^2 fitted to a hyperbolic function.

Table 1 Emission quantum yields (Φ_{em}), luminescence decay times (τ) in Ar-saturated suspensions, anisotropy at time zero (r_0), and hydrodynamic diameters obtained from TEM (D_{TEM}), anisotropy (D_{AN}), and DLS (D_{DLS}) measurements, $^1O_2$ physical quenching rate constants in toluene suspensions ($k_{1_{O_2}}$), and SiNP binding constants to BSA (K_{BSA}).

	NH$_2$SiNP	PEG–NHSiNP	Fo–NHSiNP
Φ_{em} (350 nm exc.)	0.020	0.025	0.008 0.004 (390 nm exc.)
τ (ns) (% em. light)	10.2 (60) 4.2 (40)	11.4 (44) 3.8 (56)	8.3 (74) 4.2 (26)
r_0^*	0.16 ± 0.02	0.18 ± 0.02	—
D_{TEM} (nm)	1.6 ± 0.6	—	—
D_{AN} (nm)*	1.6	1.8	—
D_{DLS}/(nm) (% v/v)	230 ± 45 (100)	140 ± 30 (12) 1700 ± 500 (33) 5250 ± 750 (54)	36 ± 9 (73) 210 ± 70 (27)
$k_{1_{O_2}}$ (M^{-1}·s^{-1})**	(2 ± 0.2) × 10^9	(2.1 ± 0.5) × 10^8	—
K_{BSA} (M^{-1})	(2 ± 1) × 10^4	(4 ± 2) × 10^3	(1.5 ± 1) × 10^4

Unless otherwise indicated, values were obtained from experiments with air-saturated aqueous phosphate buffer particle suspensions at pH = 7.0. *Anisotropy experiments corresponding to the major contributing species emitting at 450 nm. **Experiments performed in toluene suspensions.

concentration in suspensions to be estimated. These values are necessary to determine the magnitude of the effects of surface groups on particle properties, including toxicity.

Optimized SiNP geometries exhibit diameters in the range of 0.7–2.2 nm. The number of surface or terminal Si atoms ($N_{\text{Si-term}}$) was determined according to their coordination numbers. Atoms with coordination numbers equal to 1, 2, or 3 were considered as candidates for functionalization. Figure 3(b) shows the dependence of $N_{\text{Si-term}}$ on the squared diameter of the NP (D^2); the solid line in the figure represents the fitting of $N_{\text{Si-term}}$ to the function $189.6 \times D^2/(5.345 + D^2)$.

Based on this equation and an average particle diameter of 1.6 nm, it was determined that an average of 61–62 terminal Si atoms per particle were available for functionalization.

The average molar mass of the particles' Si core ($M_{\text{Si-core}} = 3{,}010$ g) was estimated by assuming a spherical 1.6-nm-size particle with a Si density of 2.33 g·cm^{-3}, in accordance with the density of bulk Si crystals. The average mass of a mole of NH$_2$SiNP ($M_{\text{NH}_2\text{SiNP}}$) was estimated by assuming that 62 terminal Si atoms of the 1.6-nm particle were functionalized with propylamine, as supported by FTIR, XPS, and surface charge data indicating a significant degree of functionalization.

Therefore, the value M_{NH_2SiNP} = 6,606 g and experimentally determined weight of dried residue from a 1-l volume of NH$_2$SiNP aqueous suspension (w_r) were used to calculate the molar concentration of the particle suspension as NH$_2$SiNP = w_r/M_{NH_2SiNP}. Even if 75% of surface Si atoms were attached to propylamine and the remainder bonded to HO groups, based on the fact that Si–H surface groups are unstable in air-saturated aqueous suspensions [1], the error in the determination of [NH$_2$SiNP] would be predicted to be on the order of 10%.

A similar procedure was applied to determine the molar concentration of PEG–NHSiNP. In this case, time-resolved anisotropy experiments indicated a low percent coverage of NH$_2$SiNP particles with PEG chains. Therefore, $M_{PEG–NH_2SiNP}$ = 8,900 g was estimated assuming a 6% functionalization of NH$_2$SiNP terminal amino groups. Given that the expected surface coverage was in the range of 10%–1.5%, the error in the determination of [PEG–NHSiNP] was on the order of 25%.

3.3 Photoluminescence properties

Bare and surface-modified SiNPs exhibited photoluminescence in the wavelength range of 250–600 nm. The dependence of the emission spectrum on the excitation wavelength indicated the contribution of various families of emitters due to differences in particle size, agglomeration, and/or surface morphology and chemistry [21]. Therefore, a bilinear regression analysis of the emission–excitation matrix was performed to determine the minimum number of species contributing to the overall emission.

NH$_2$SiNP suspensions at pH = 7.0 showed a major contribution of species with an excitation–emission maximum (λ_{exc} (nm), λ_{em} (nm)) at (360, 450), with a less significant contribution of species emitting at (450, 500) (Figs. 4(a) and 4(b)). PEG–NHSiNP also shows a major contribution of species with (λ_{exc} (nm), λ_{em} (nm)) at (360, 450), with a less significant contribution of emitters at (430–450, 500). Excluding their relative contributions to overall luminescence, these species were in agreement with those observed for NH$_2$SiNP.

Surface coverage with PEG did not change the shape of excitation–emission spectra, suggesting a common origin of the luminescence. Therefore, the observed
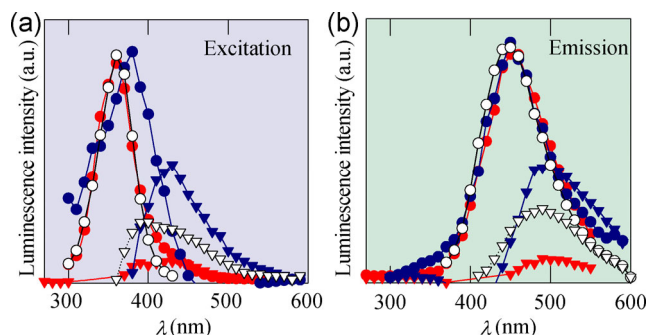

Figure 4   Excitation and emission spectra (left and right panels, respectively) of contributing species obtained from a bilinear analysis of the emission–excitation matrix of NH$_2$SiNP (red), Fo–NHSiNP (blue), and PEG–NHSiNP (white) aqueous suspensions (0.01 M and pH = 7.0). For comparison, the excitation–emission spectrum of each particle was arbitrarily normalized to the emission at 450 nm. However, the intensity ratio between the two families of emitting species of each particle was maintained to show their relative contribution to overall luminescence.

increase in contribution of species emitting at around 500 nm could not be attributed to an increase in the concentration of particles of different size, geometry and/or surface morphology, since both NH$_2$SiNP and PEG–NHSiNP were from the same synthesis batch. However, since larger aggregates were observed by DLS for PEG–NHSiNP than for NH$_2$SiNP (Table 1), it was speculated that aggregation may have affected the 500-nm emission, as previously reported for SiNP [21] and CdSe nanocrystals [34].

Time-domain anisotropy experiments were performed by exciting with a 388-nm light and detecting the emission at 430 nm in order to identify the major species contributing to overall luminescence. Anisotropy profiles obtained for NH$_2$SiNP and PEG–NHSiNP were described by a single exponential, with $r(t) = r_0 \times \exp(−t/\theta)$. The rotational correlation time (θ) and anisotropy at time zero (r_0) are shown in Table 1. The single exponential was consistent with emission primarily originating from a population of particles with three identical perpendicular rotational axes, suggesting a spherical form. The time for Brownian rotation of a molecule (θ) provides information on the hydrodynamic diameter (D) based on the Stokes–Einstein–Debye equation. Considering the shear viscosity of water at 300 K (η = 1.00 mPa·s), D = 1.6 nm was obtained for NH$_2$SiNP which, within experimental error, was consistent with TEM data. In fact, the

broad photoluminescence bands (FWHM of about $\Delta E \approx 500$ meV) and decay lifetimes in the nanosecond range (Table 1) were in agreement with those reported for 1–2 nm Si core particles [35]. On the other hand, PEG–NHSiNP showed slightly higher D values (1.8 nm). An estimate of particle size after functionalization with PEG was obtained by assuming that the polymer retained a random coil structure after covalent linking to the particle surface [4]. The gyration radius, $R_g = (n \times \ell/6)^{1/2}$—where $n = 14$ and $\ell = 3.1$ Å are the number and length of oxyethylene units, respectively, assumed as rigid segments of the PEG chain—was ~5 Å. Therefore, predicted sizes of highly covered PEG–NHSiNPs were 2.6–3.6 nm. The fact that the measured $D = 1.8$ nm was smaller than the predicted value could indicate that grafted PEG chains lie almost parallel to the particle surface, a conformation made possible by low coverage.

Moreover, r_0 values of 0.16 and 0.18 obtained for NH$_2$SiNP and PEG–NHSiNP, respectively, were considered to be within the 10% experimental error. These values suggest different orientations for absorption and emission transition moments of the particle, and are in agreement with the large Stokes shifts between excitation and emission spectra. Moreover, the concurrence between the r_0 values of NH$_2$SiNP and PEG–NHSiNP confirms that PEG functionalization does not modify NH$_2$SiNP electronic states.

Table 1 also lists emission quantum yields obtained at 350 nm excitation (Φ_{em}) in air-saturated aqueous suspensions at pH = 7.0 for the three synthesized particles. The emission quantum yield of NH$_2$SiNP was 10 times smaller than that reported in toluene suspensions [12], possibly because the surrounding medium had a profound effect on particle photophysics [3]. The ~25% higher Φ_{em} observed for PEG–NHSiNP than for NH$_2$SiNP may be due to the surface protection conferred by attached PEG molecules.

The luminescence intensity—but not spectrum shape—of NH$_2$SiNP and PEG–NHSiNP was dependent on the presence of dissolved molecular oxygen, with a ~10% difference in intensity observed between argon- and air-saturated aqueous suspensions. Oxygen quenching is reversible, since the luminescence is recovered upon displacement of oxygen with argon.

The excitation–emission matrix of Fo–NHSiNP also revealed the contribution of the two main families of emitters. The major contributing species with (λ_{exc} (nm), λ_{em} (nm)) at (380, 450) showed an emission spectrum closely resembling that of NH$_2$SiNP, although the excitation spectrum was shifted ~ 20 nm towards the red range. A similar shift was reported upon covalent binding of Fo to graphene oxide [6]. A second family of species with (λ_{exc} (nm), λ_{em} (nm)) at (430, 490) also contributed to the overall luminescence. Anisotropy experiments showed extremely noisy and rapid depolarized signals that could not be analyzed within the time resolution of our experimental set-up. These trends, as well as the lower Φ_{em} and smaller aggregate sizes measured for the particles (Table 1) suggest a perturbation of NH$_2$SiNP electronic states due to covalent binding of Fo.

3.4 Singlet oxygen generation

SiNPs are well-known $^1O_2$ photosensitizers [1, 2, 36–38]. The effect of surface derivatization on $^1O_2$ photosensitizing capacity was evaluated in two sets of experiments using continuous and pulsed irradiation.

3.4.1 Time-resolved detection of $^1O_2$ luminescence at 1,270 nm

Air-saturated toluene and D$_2$O suspensions of NH$_2$SiNP, Fo–NHSiNP, and PEG–NHSiNP excited with 355-nm laser showed no emission traces at 1270 nm. However, $^1O_2$ traces generated upon 355-nm irradiation of DPA solutions were quenched by adding the particles (NH$_2$SiNP shown in Fig. 5 inset). Fitting an exponential decay function to $^1O_2$ traces yielded information on the lifetime of $^1O_2$ in the presence (τ_Δ) and absence (τ_Δ^0) of SiNPs. A Stern-Volmer plot of the inverse of $^1O_2$ lifetimes vs. [SiNP] (Eq. (1)) yielded $^1O_2$ quenching rate constants of the particles ($k_0 = k_4 + k_5$) due to physical and reactive mechanisms (described by reactions (4) and (5) in Fig. 5, respectively) [39]. A value of $\tau_\Delta^0 = 31$ μs was obtained, in agreement with values reported in toluene [40]. The slopes of the lines of τ_Δ^{-1} vs. [SiNP] shown in Fig. 5 yielded $^1O_2$ quenching constants ($k_4 + k_5$) of $(2 \pm 0.2) \times 10^9$ and $(2.1 \pm 0.5) \times 10^8$ M^{-1}·s^{-1} for NH$_2$SiNP and PEG–NHSiNP in toluene, respectively.
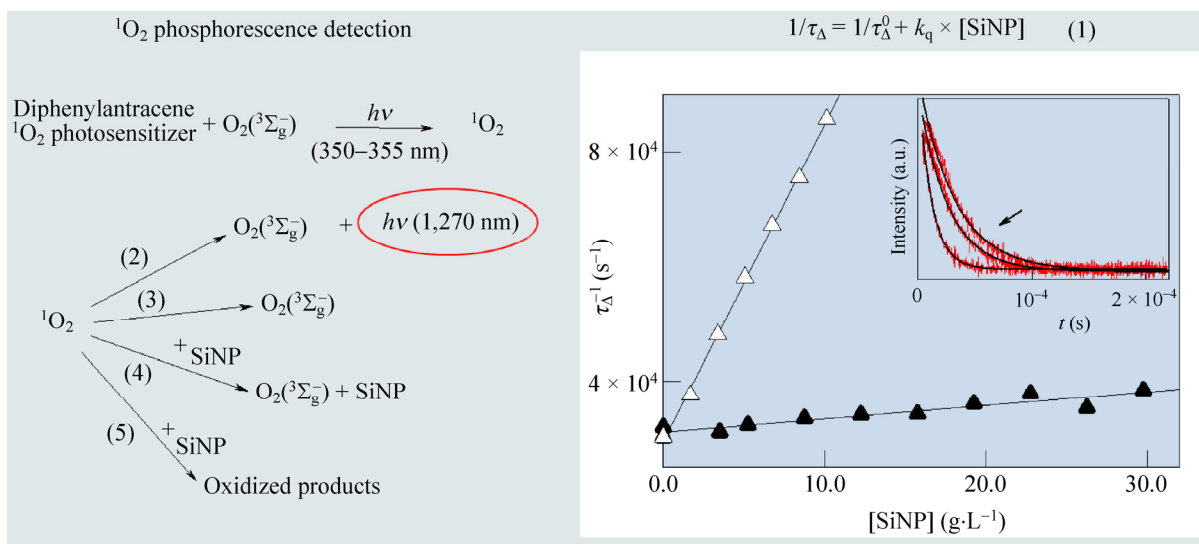
Figure 5 Plots of τ_Δ^{-1} vs. [SiNP] for (Δ) NH$_2$SiNP and (▲) PEG–NHSiNP. Inset: $^1O_2$ near-infrared phosphorescence traces at 1,270 nm obtained upon excitation at 355 nm of 9,10-DPA in air-saturated toluene solution (upper curve) and after addition of 4.2×10^{-4} and 2.5×10^{-3} g·L^{-1} NH$_2$SiNP (succeeding curves in the direction of the arrow). Black lines indicate the curve fitted to a single exponential decay equation. The reactions in each experiment are also shown.

3.4.2 Detection of O_2 consumption in continuous irradiation experiments

SiNP suspensions were irradiated with a 350-nm light in the presence and absence of specific $^1O_2$ scavengers, i.e., FFA and sodium azide (N$_3^-$) [36]. Irradiation of air-saturated aqueous suspensions of either NH$_2$SiNP or PEG–NHSiNP showed no O_2 depletion (Fig. 6 inset). However, the addition of 10^{-3} M FFA to the particle suspension resulted in O_2 depletion. Since FFA is a well-known chemical scavenger of $^1O_2$ (reaction (7) in Fig. 6), the latter observations strongly support the capacity of NH$_2$SiNP and PEG–NHSiNP to produce $^1O_2$ upon 350-nm irradiation. To test this assumption, a physical quencher of $^1O_2$, i.e., N$_3^-$ (reaction (6)) was added in excess, which was expected to diminish the rate of O_2 depletion due to the competition of N$_3^-$ with FFA for $^1O_2$, as observed experimentally. In the absence of chemical $^1O_2$ quenchers, no molecular oxygen consumption was expected due to efficient relaxation of $^1O_2$ to $^3O_2$ (reactions (2) and (3)). These observations provide evidence for the production of $^1O_2$ upon irradiation of NH$_2$SiNP and PEG–NHSiNP, as well as a negligible chemical reaction between $^1O_2$ and the particle surface ($k_{5,\text{NH}_2\text{SiNP}}$ and $k_{5,\text{PEG–NHSiNP}} < 10^3$ M^{-1}·s^{-1}). Therefore, the efficient quenching of $^1O_2$ phosphorescence by NH$_2$SiNP and PEG–NHSiNP mainly occurred

via a physical interaction, yielding $k_{4,\text{NH}_2\text{SiNP}} = (2 \pm 0.2) \times 10^9$ M^{-1}·s^{-1} and $k_{4,\text{PEG–NHSiNP}} = (2.1 \pm 0.5) \times 10^8$ M^{-1}·s^{-1}. In fact, NH groups are known to support the relaxation of $^1O_2$ to the ground state [41]. The individual contribution of propylamine groups to the overall quenching would yield a rate constant of 3×10^7 M^{-1}·s^{-1} per propylamine group, which is almost two orders of magnitude higher than that reported for the propylamine molecule, but on the order of amines capable of stabilizing a $[^1O_2^{\delta-} \cdots N^{\delta+} R_3]$ partial charge transfer intermediate [40]. The enhanced quenching efficiency by propylamine groups grafted to SiNPs suggests a stabilized charge transfer intermediate via chemical bonding to Si. These observations are consistent with the diminished $^1O_2$ photosensitization efficiency of propylamine-terminated, hydrophilic porous Si compared to the surface-oxidized material [38]. On the other hand, the smaller quenching constant observed for PEGylated particles suggest a protective effect exerted by PEG against the particle's reactivity towards $^1O_2$.

Experiments performed with Fo–NHSiNP showed O_2 depletion as a function of irradiation time in the absence of $^1O_2$ scavengers. The addition of 10^{-3} M FFA resulted in further O_2 depletion, which was partially restored upon addition of excess N$_3^-$. These results
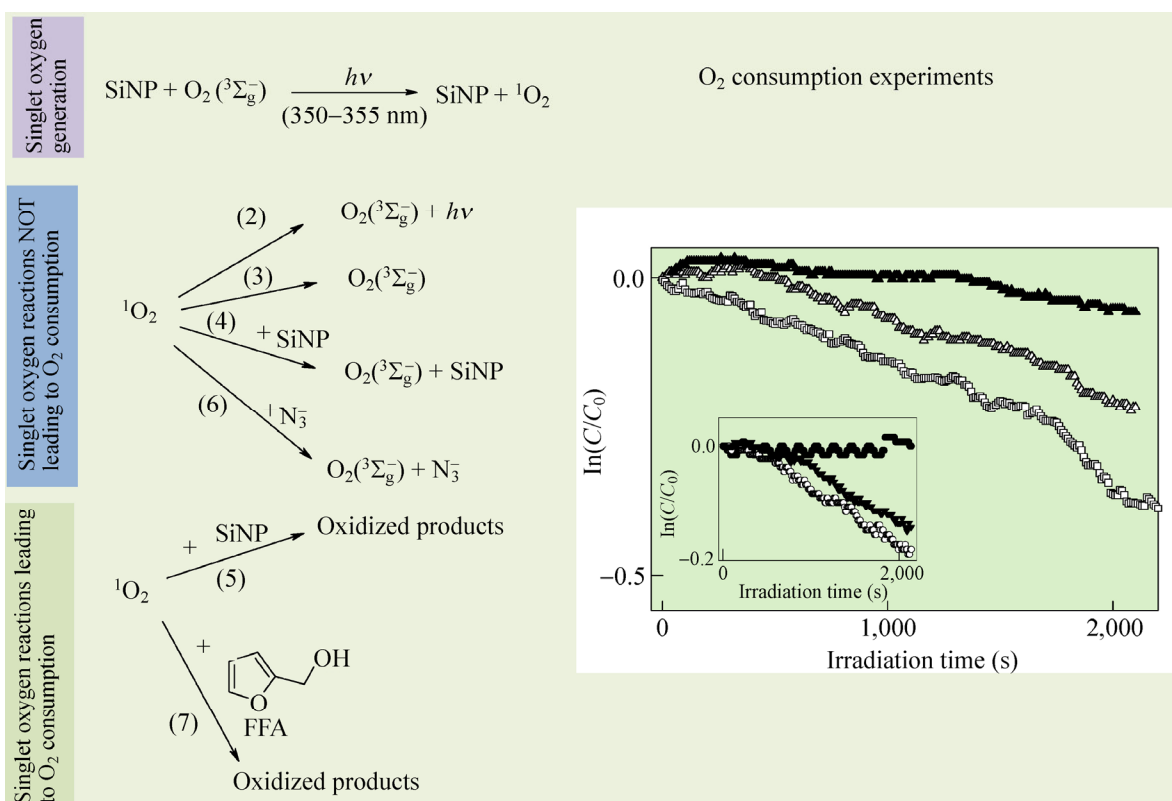
Figure 6 O_2 consumption during 350-nm irradiation of air-saturated aqueous suspensions of PEG–NHSiNP (▲), PEG–NHSiNP with 10^{-3} M FFA (△), and Fo–NHSiNP with 10^{-3} M FFA (□). Inset: Main figure for NH_2SiNP (●), NH_2SiNP with 10^{-3} M FFA (O), and NH_2SiNP with 10^{-3} MFFA and 10^{-2} M azide (▼). The reactions in each experiment are also shown.

provide evidence of $^1O_2$ generation. As previously discussed, O_2 depletion in the absence of scavengers could indicate the chemical reaction of $^1O_2$ with particle surface groups. Fo is known to quench $^1O_2$ physically (rate constant of $k_T = 3.0 \times 10^7$ $M^{-1}\cdot s^{-1}$) [42] and chemically (rate constant of $k_r = 2.8 \times 10^6$ $M^{-1}\cdot s^{-1}$) [43]. If the Fo moiety attached to the Si particle were to maintain a reactivity similar to that of solution-free Fo, then $^1O_2$ quenching by the anchored folate moiety would be mainly physical and O_2 would not be significantly consumed in the absence of $^1O_2$ chemical scavengers, contrary to the observed trend. The generation of superoxide radical anion (O_2^-) involving electron transfer from photoexcited particles to O_2 is among the possible O_2-consuming reactions that occur, as reported for surface-oxidized SiNPs [1].

3.5 O_2^- generation

Since O_2^- recombination leads to H_2O_2 production, a commercial enzymatic colorimetric assay was used to measure $[H_2O_2]$ as an indirect method for determining O_2^- generation. H_2O_2 formation was primarily observed in irradiation experiments with aqueous suspensions of Fo–NHSiNP ($\sim 1.3 \times 10^{-4}$ M), while negligible amounts were detected ($< 1 \times 10^{-5}$ M) in experiments with NH_2SiNP and PEG–NHSiNP. The different behavior observed for Fo–NHSiNP further supports the involvement of Fo complex photophysics in the photophysical/photochemical processes of Fo–NHSiNP.

3.6 Interaction with FBS proteins

The addition of FBS to NH_2SiNP and PEG–NHSiNP aqueous suspensions enhanced the luminescence intensity of the particles without altering spectrum shape (NH_2SiNP shown in Fig. 7(a)). On the other hand, adding NH_2SiNP, PEG–NHSiNP, or Fo–NHSiNP to FBS aqueous solutions decreased the intensity of tryptophan fluorescence (maximum emission of 345–350 nm at 290–300 nm excitation) without shifting the emission band (Fig. 7(b)). The fluorescence decay of tryptophan
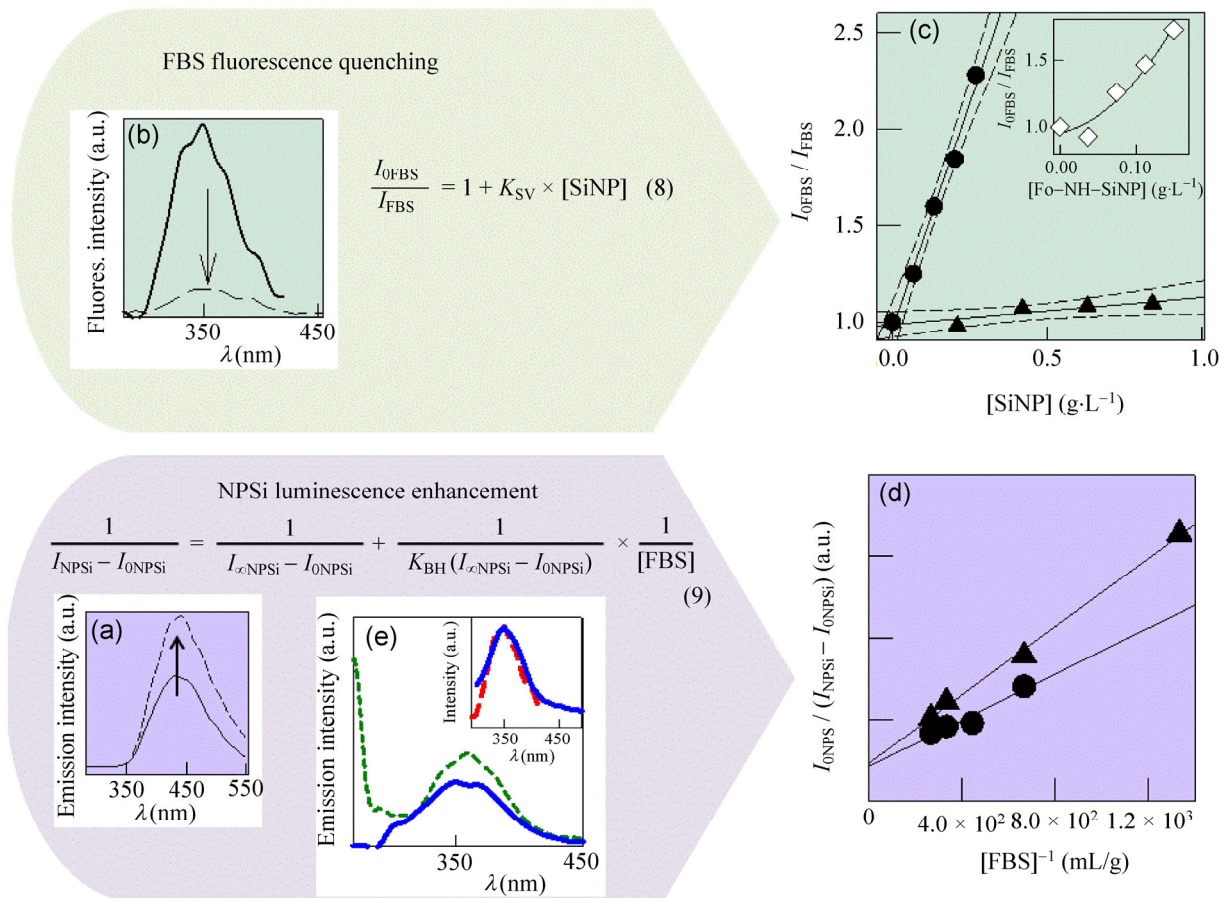
Figure 7 (a) Emission spectra (350 nm excitation) of 1.9×10^{-5} M NH$_2$SiNP in the absence (solid line) and presence of 10% FBS (broken line). (b) Fluorescence emission (300 nm excitation) of tryptophan residues in 10% FBS before (solid line) and after (broken line) 1.9×10^{-5} M NH$_2$SiNP addition. (c) Plot of I_{0FBS}/I_{FBS} vs. [NH$_2$SiNP] (●) or [PEG–NHSiNP] (▲). Inset: Main figure for Fo–NHSiNP (◊). (d) Plots of $(I_{NPSi} - I_{0NPSi})^{-1}$ vs. [FBS]$^{-1}$ were normalized to I_{0NPSi}. (●) and (▲) represent experiments with NH$_2$SiNP and PEG–NHSiNP, respectively. (e) Excitation spectrum (450 nm detection) of NH$_2$SiNP in the absence (solid blue line) and after addition of 10% FBS (broken green line). Inset: Fluorescence emission (280 nm excitation) of 10% FBS solution (red curve) and excitation spectrum (450 nm detection) of NH$_2$SiNP (blue curve). Experiments were performed with phosphate buffer suspensions at pH = 7.0.

residues was fitted to a bi-exponential decay equation with decay times $\tau_1 = 1.88 \pm 0.03$ ns and $\tau_2 = 6.60 \pm 0.03$ ns, which were unaffected (within the experimental error) by the addition of NH$_2$SiNP and PEG–NHSiNP, suggesting a static quenching due to the formation of BSA ground state complexes with NH$_2$SiNP and PEG–NHSiNP, respectively [44]. The stabilization of NPs by bovine or human SA [45] has been ascribed to the hydrophobic environment created by these proteins [46, 47]. On the other hand, the surface stabilization of SiNP by hydrophobic solvents and organic coverage has been shown to increase SiNP photoluminescence [12]. Therefore, the observed results strongly support an interaction between FBS protein structure and SiNPs. It was recently reported that the formation of

propylamine abolished Si quantum dots:BSA ground state complexes [48].

The quenching of luminescence intensity of tryptophan residues by the addition of SiNP was described by the Stern–Volmer equation (8), where I_{0FBS} and I_{FBS} are the integrated fluorescence intensities (areas under the fluorescence curves) in the absence and presence of NPs, respectively, corrected for inner filter effects [44], and K_{SV} is the Stern–Volmer quenching constant. The ratio I_{0FBS}/I_{FBS} showed a linear dependence with particle concentration (Fig. 7(c)), consistent with a static mode as the main quenching process. Therefore, tryptophan residues and SiNPs were bound to the same protein within quenching distances, with K_{SV} representing the SiNP:BSA binding constant. The

slope of the plot yielded $K_{SV} = (3.1 \pm 0.3) \times 10^4$ M^{-1} for NH$_2$SiNP:BSA ground state complexes, which is on the order reported for the interaction of most molecules with albumin [44], and $K_{SV} = (1.3 \pm 0.4) \times 10^3$ M^{-1} for PEG–NHSiNP:BSA complexes. The lower binding constant observed for PEG–NHSiNP indicated diminished binding within the quenching distance.

Since NH$_2$SiNP and PEG–NHSiNP fluorescence increased with the addition of increasing amounts of FBS at excitation wavelengths where FBS does not absorb (i.e., 350 nm), the binding interaction was also studied using the double reciprocal plot following the Benesi–Hildebrand equation (9), where I_{0NPSi}, I_{NPSi}, and $I_{\infty NPSi}$ are the integrated fluorescence intensities of SiNPs in the absence of protein, at an intermediate protein concentration, and at a concentration producing total interaction, respectively. The binding constant K_{BH} was obtained from the slope and ordinate of the linear plots of $(I_{NPSi} - I_{0NPSi})^{-1}$ vs. [FBS]$^{-1}$ for NH$_2$SiNP and PEG–NHSiNP (Fig. 7(d)).

Given that commercial FBS is 3.0%–4.5% total protein and assuming that albumin is the main constituent protein [49], binding constants of $(2 \pm 1) \times 10^4$ and $(4 \pm 2) \times 10^3$ M^{-1} were estimated for NH$_2$SiNP and PEG–NHSiNP, respectively. These values were on the order of binding constants obtained from the fluorescence quenching experiments, suggesting that the increase in luminescence of NH$_2$SiNP and PEG–NHSiNP is related to the formation of SiNP:BSA ground state complexes.

Fo–NHSiNP luminescence was not enhanced by adding increasing amounts of FBS. However, adding Fo–NHSiNP to FBS solutions quenched the fluorescence and decay times of tryptophan residues (i.e., $\tau_1 = 1.38 \pm 0.03$ ns and $\tau_1 = 5.55 \pm 0.03$ ns in the presence of 0.075 g·L^{-1} Fo–NHSiNP). Dynamic and static interactions of Fo–NHSiNP with BSA were responsible for the upward curvature observed in the Stern–Volmer plot (Fig. 7(c) inset). The K_{SV} of $(1.5 \pm 1) \times 10^4$ M^{-1} was on the order calculated for NH$_2$SiNP:BSA ground state complexes.

The observation that the tryptophan emission and particle excitation spectra overlap (shown for NH$_2$SiNP in Fig. 7(e) inset) implies the occurrence of resonance energy transfer (RET) between tryptophan (donor) and SiNP (acceptor). In fact, the appearance of the tryptophan excitation spectrum during detection of NH$_2$SiNP emission in NH$_2$SiNP–FBS mixtures (Fig. 7(e)) indicated RET between BSA tryptophan residues and NH$_2$SiNP. However, this behavior was not observed for FBS mixtures with Fo–NHSiNP and PEG–NHSiNP, suggesting that RET was negligible in these systems. Considering that all three particles would be expected to show similar capacity for energy transfer, the latter observations indicate that BSA:SiNP interactions strongly depend on the particle's surface coverage, since Fo–NHSiNP and PEG–NHSiNP are not located within RET distances.

4 Conclusions

Propylamine-functionalized particles (NH$_2$SiNP) may be used as intermediates for surface derivatization involving amide links. At physiological pH, NH$_2$SiNPs showed positive surface charges and formed stable, highly dispersed aqueous suspensions. NH$_2$SiNPs bound to tryptophan residues of BSA within quenching distance, leading to a net increase in particle luminescence and to RET. Collectively, these properties open new opportunities for the application of NH$_2$SiNP as luminescent sensors in biological systems based on RET.

Surface functionalization of NH$_2$SiNP with PEG did not modify the luminescence properties of the particles, but reduced the surface charge with a consequent increase in the size of particle aggregates. The binding of PEG–NHSiNP to BSA was one order of magnitude lower than that of NH$_2$SiNP. Since protein adsorption is the preliminary step for immune system recognition by macrophages, PEG grafting to SiNPs is a good strategy for reducing protein adsorption. On the other hand, NH$_2$SiNP functionalization with Fo yielded a negatively charged surface at physiological pH, diminished luminescence quantum yield, and a capacity for O_2^- production upon light irradiation.

The results of this study clearly indicate that surface coating with propylamine decreases the $^1O_2$-photosensitizing capacity of particles as compared to surface-oxidized derivatives due to the enhanced quenching properties of propylamine groups attached to SiNPs. PEG-functionalized particles reduce protein

adhesion; however, their $^1O_2$-quenching ability precludes their use as $^1O_2$ photosensitizers. Functionalization with Fo, which shows greater capacity for O_2^- production, is potentially useful for photodynamic therapy.

The present study provides insight into the effects of surface coating on the photophysical properties and photosensitizing capacity of SiNPs, which is essential for therapeutic and sensing applications. The important parameters obtained in the present work, i.e., emission quantum yields, luminescence decay times, anisotropy at time zero, hydrodynamic diameters, $^1O_2$ physical quenching rate constants, and SiNP binding constants to BSA are summarized in Table 1.

Acknowledgements

References

[1] Llansola Portolés, M. J.; David Gara, P. M.; Kotler, M. L.; Bertolotti, S.; San Román, E.; Rodríguez, H. B.; Gonzalez, M. C. Silicon nanoparticle photophysics and singlet oxygen generation. *Langmuir* **2010**, *26*, 10953–10960.

[2] Burda, C.; Chen, X. B.; Narayanan, R.; El-Sayed, M. A. Chemistry and properties of nanocrystals of different shapes. *Chem. Rev.* **2005**, *105*, 1025–1102.

[3] Llansola Portolés, M. J.; Rodriguez Nieto, F.; Soria, D. B.; Amalvy, J. I.; Peruzzo, P. J.; Mártire, D. O.; Kotler, M.; Holub, O.; Gonzalez, M. C. Photophysical properties of blue-emitting silicon nanoparticles. *J. Phys. Chem. C* **2009**, *113*, 13694–13702.

[4] Sperling, R. A.; Parak, W. J. Surface modification, functionalization and bioconjugation of colloidal inorganic nanoparticles. *Phil. Trans. R. Soc. A* **2010**, *368*, 1333–1383.

[5] Wang, C. H.; Liu, C. J.; Wang, C. L.; Huang, T. E.; Obliosca, J. M.; Lee, K. H.; Hwu, Y.; Yang, C. S.; Liu, R. S.; Lin, H. M. et al. Optimizing the size and surface properties of polyethylene glycol (PEG)–gold nanoparticles by intese X-ray irradiation. *J. Phys. D: Appl. Phys.* **2008**, *41*, 195301.

[6] Matsumura, Y.; Maeda, H. A new concept for macromolecular therapeutics in cancer chemotherapy: Mechanism of tumoritropic accumulation of proteins and the antitumor agent smancs. *Cancer Res.* **1986**, *46*, 6387–6392.

[7] Paciotti, G. F.; Kingston, D. G. I.; Tamarkin, L. Colloidal gold nanoparticles: A novel nanoparticle platform for developing multifunctional tumor-targeted drug delivery vectors. *Drug. Develop. Res.* **2006**, *67*, 47–54.

[8] David Gara, P.; Garabano, N.; Llansola Portoles, M.; Moreno, M. S.; Dodat, D.; Casas, O.; Gonzalez, M.; Kotler, M. ROS enhancement by silicon nanoparticles in X-ray irradiated aqueous suspensions and in glioma C6 cells. *J. Nanopart. Res.* **2012**, *14*, 741.

[9] Klein, S.; Dell'Arciprete, M. L.; Wegmann, M.; Distel, L. V. R.; Neuhuber, W.; Gonzalez, M. C.; Kryschi, C. Oxidized silicon nanoparticles for radiosensitization of cancer and tissue cells. *Biochem. Bioph. Res. Commun.* **2013**, *434*, 217–222.

[10] Huang, P.; Xu, C.; Lin, J.; Wang, C.; Wang, X. S.; Zhang, C. L.; Zhou, X. J.; Guo, S. W.; Cui, D. X. Folic acid-conjugated graphene oxide loaded with photosensitizers for targeting photodynamic therapy. *Theranostics* **2011**, *1*, 240–250.

[11] Lu, Y. J.; Low, P. S. Folate-mediated delivery of macromolecular anticancer therapeutic agents. *Adv. Drug Deliver. Rev.* **2002**, *54*, 675–693.

[12] Romero, J. J.; Llansola Portolés, M. J.; Dell'Arciprete, M. L.; Rodríguez, H. B.; Moore, A. L.; Gonzalez, M. C. Photoluminescent 1–2 nm sized silicon nanoparticles: A surface-dependent system. *Chem. Mater.* **2013**, *25*, 3488–3498.

[13] Bhattacharjee, S.; Rietjens, I. M. C. M.; Singh, M. P.; Atkins, T. M.; Purkait, T. K.; Xu, Z. J.; Regli, S.; Shukaliak, A.; Clark, R. J.; Mitchell, B. S. et al. Cytotoxicity of surface-functionalized silicon and germanium nanoparticles: The dominant role of surface charges. *Nanoscale* **2013**, *5*, 4870–4883.

[14] Nel, A. E.; Mädler, L.; Velegol, D.; Xia, T.; Hoek, E. M. V.; Somasundaran, P.; Klaessig, F.; Castranova, V.; Thompson, M. Understanding biophysicochemical interactions at the nano-bio interface. *Nat. Mater.* **2009**, *8*, 543–557.

[15] Erogbogbo, F.; Tien, C. A.; Chang, C. W.; Yong, K. T.; Law, W. C.; Ding, H.; Roy, I.; Swihart, M. T.; Prasad, P. N. Bioconjugation of luminescent silicon quantum dots for selective uptake by cancer cells. *Bioconjugate Chem.* **2011**, *22*, 1081–1088.

[16] Doshi, N.; Mitragotri, S. Designer biomaterials for nanomedicine. *Adv. Funct. Mater.* **2009**, *19*, 3843–3854.

[17] Ausubel, F. M.; Brent, R.; Kingston, R. E.; Seidman, J. G.; Smith, J. A.; Struhl, K. *Current Protocols in Molecular Biology.* John Wiley & Sons: New York, 2003.

[18] Lakowicz, J. R. *Principles of Fluorescence Spectroscopy*, 3rd ed.; Springer Science+Business Media: New York, 2006.

[19] Frauenheim, T.; Seifert, G.; Elstner, M.; Niehaus, T.; Köhler, C.; Amkreutz, M.; Sternberg, M.; Hajnal, Z.; Di Carlo, A.; Suhai, S. Atomistic simulations of complex materials: Ground-state and excited-state properties. *J. Phys.: Condens. Matter* **2002**, *14*, 3015–3047.

[20] Steinbeck, M. J.; Khan, A. U.; Karnovsky, M. J. Extracellular production of singlet oxygen by stimulated macrophages quantified using 9,10-diphenylanthracene and perylene in a polystyrene film. *J. Biol. Chem.* **1993**, *268*, 15649–15654.

[21] Llansola Portolés, M. J.; Pis Diez, R.; Dell'Arciprete, M. L.; Caregnato, P.; Romero, J. J.; Mártire, D. O.; Azzaroni, O.; Ceolín, M.; Gonzalez, M. C. Understanding the parameters affecting the photoluminescence of silicon nanoparticles. *J. Phys. Chem. C* **2012**, *116*, 11315–11325.

[22] Warner, J. H.; Hoshino, A.; Yamamoto, K.; Tilley, R. D. Water-soluble photoluminescent silicon quantum dots. *Angew. Chem.* **2005**, *117*, 4626–4630.

[23] Atkins, T. M.; Louie, A. Y.; Kauzlarich, S. M. An efficient microwave-assisted synthesis method for the production of water soluble amine-terminated Si nanoparticles. *Nanotechnology* **2012**, *23*, 294006.

[24] Hua, F. J.; Swihart, M. T.; Ruckenstein, E. Efficient surface grafting of luminescent silicon quantum dots by photoinitiated hydrosilylation. *Langmuir* **2005**, *21*, 6054–6062.

[25] Elstner, M.; Porezag, D.; Jungnickel, G.; Elsner, J.; Haugk, M.; Frauenheim, T.; Suhai, S.; Seifert, G. Self-consistent-charge density-functional tight-binding method for simulations of complex materials properties. *Phys. Rev. B* **1998**, *58*, 7260–7268.

[26] Aradi, B.; Hourahine, B.; Frauenheim, T. DFTB+, a sparse matrix-based implementation of the DFTB method. *J. Phys. Chem. A* **2007**, *111*, 5678–5684.

[27] Rosso-Vasic, M.; Spruijt, E.; van Lagen, B.; De Cola, L.; Zuilhof, H. Alkyl-functionalized oxide-free silicon nano-particles: Synthesis and optical properties. *Small* **2008**, *4*, 1835–1841.

[28] Wilcoxon, J. P.; Samara, G. A.; Provencio, P. N. Optical and electronic properties of Si nanoclusters synthesized in inverse micelles. *Phys. Rev. B* **1999**, *60*, 2704–2714.

[29] Wahab, M. A.; Kim, I.; Ha, C. S. Bridged amine-functionalized mesoporous organosilica materials from 1,2-bis(triethoxysilyl)ethane and bis[(3-trimethoxysilyl) propyl]amine. *J. Solid. State Chem.* **2004**, *177*, 3439–3447.

[30] Coates, J. Interpretation of infrared spectra, a practical approach. In *Encyclopedia of Analytical Chemistry*. Meyer, R. A., Ed. John Wiley & Sons Ltd: Chinchester, 2000; pp10815–10837.

[31] Alexander, M. R.; Short, R. D.; Jones, F. R.; Michaeli, W.; Blomfield, C. J. A study of HMDSO/O_2 plasma deposits using a high-sensitivity and -energy resolution XPS instrument: Curve fitting of the Si 2p core level. *Appl. Surf. Sci.* **1999**, *137*, 179–183.

[32] Hairdary, S. M.; Córcoles, E. P.; Ali, N. K. Folic acid delivery device based on porous silicon nanoparticles synthesized by electrochemical etching. *Int. J. Electrochem. Sci.* **2013**, *8*, 9956–9966.

[33] Wu, Z. P.; Zuo, F.; Zheng, Z. H.; Ding, X. B.; Peng, Y. X. A novel approach to molecular recognition surface of magnetic nanoparticles based on host–guest effect. *Nanoscale Res. Lett.* **2009**, *4*, 738–747.

[34] Mattoussi, S. H.; Cumming, A. W.; Murray, C. B.; Bawendi, M. G. Properties of CdSe nanocrystal dispersions in the dilute regime: Structure and interparticle interactions. *Phys. Rev. B* **1998**, *58*, 7850–7863.

[35] Smith, A.; Yamani, Z. H.; Roberts, N.; Turner, J.; Habbal, S. R.; Granick, S.; Nayfeh, M. H. Observation of strong direct-like oscillator strength in the photoluminescence of Si nanoparticles. *Phys. Rev. B* **2005**, *72*, 205307.

[36] Xiao, L.; Gu, L.; Howell, S. B.; Sailor, M. J. Porous silicon nanoparticle photosensitizers for singlet oxygen and their phototoxicity against cancer cells. *ACS Nano* **2011**, *5*, 3651–3659.

[37] Timoshenko, V. Light-induced generation of singlet oxygen in porous silicon. In *Sensors for Environment, Health and Security*. Baraton, M. I., Ed. Springer: the Netherlands, 2009; pp125–139.

[38] Fumon, H; Nojiri, M.; Fujii, M. Hayashi, S.; Akamatsu, K. Sensitized generation of singlet oxygen by allylamine-terminated hydrophillic porous Si. *Trans. Mat. Res. Soc. Jpn.* **2008**, *33*, 165–168.

[39] Schweitzer, C.; Schmidt, R. Physical mechanisms of generation and deactivation of singlet oxygen. *Chem. Rev.* **2003**, *103*, 1685–1758.

[40] Wilkinson, F.; Helman, W. P.; Ross, A. B. Rate constants for the decay and reactions of the lowest electronically excited singlet state of molecular oxygen in solution. An expanded and revised compilation. *J. Phys. Chem. Ref. Data* **1995**, *24*, 663–677.

[41] Darmanyan, A. P.; Jenks, W. S.; Jardon, P. Charge-transfer quenching of singlet oxygen $O_2(^1\Delta_g)$ by amines and aromatic hydrocarbons. *J. Phys. Chem. A* **1998**, *102*, 7420–7426.

[42] Thomas, A. H.; Lorente, C.; Capparelli, A. L.; Martinez, C. G.; Braun, A. M.; Oliveros, E. Singlet oxygen ($^1\Delta_g$) production by pterin derivatives in aqueous solutions. *Photochem. Photobio. Sci.* **2003**, *2*, 245–250.

[43] Cabrerizo, F. M.; Laura Dántola, M.; Petroselli, G.; Capparelli, A. L.; Thomas, A. H.; Braun, A. M.; Lorente, C.; Oliveros, E. Reactivity of conjugated and unconjugated pterins with singlet oxygen ($O_2(^1\Delta_g)$): Physical quenching and chemical reaction. *Photochem. Photobiol.* **2007**, *83*, 526–534.

[44] Alarcón, E.; Aspée, A.; Abuin, E. B.; Lissi, E. A. Evaluation of solute binding to proteins and intra-protein distances from steady state fluorescence measurements. *J. Photochem. Photobiol. B* **2012**, *106*, 1–17.

[45] Rahman, M.; Laurent, S.; Tawil, N.; Yahia, L.; Mahmoundi, M. *Protein–Nanoparticle Interactions—The Bio-Nano Interface*; Springer-Verlag Berlin Heidelberg: Berlin, 2013.

[46] Ying, P. Q.; Jin, G.; Tao, Z. L. Competitive adsorption of collagen and bovine serum albumin—Effect of the surface wettability. *Colloid. Surf. B* **2004**, *33*, 259–263.

[47] Lynch, I.; Dawson, K. A. Protein–nanoparticle interactions. *Nano Today* **2008**, *3*, 40–47.

[48] Chatterjee, S.; Mukherjee, T. K. Spectroscopic investigation of interaction between bovine serum albumin and amine-functionalized silicon quantum dots. *Phys. Chem. Chem. Phys.* **2014**, *16*, 8400–8408.

[49] Valeur, B. Resonance energy transfer and its applications. In *Molecular Fluorescence: Principles and Applications*. Valeur, B., Ed.; Wiley-VCH Verlag GmbH: Weinhelm, 2001; pp247–272.